Quantitative imaging of fractures around a borehole using linear slip theory and elastic least-squares migration

Minato, Shohei; Ghose, Ranajit; Wapenaar, Kees

DOI
10.1190/segam2019-3213991.1

Publication date
2019

Document Version
Accepted author manuscript

Published in
SEG Technical Program Expanded Abstracts 2019

Quantitative imaging of fractures around a borehole using linear slip theory and elastic least-squares migration

Shohei Minato, Delft University of Technology and OYO Corporation; Ranajit Ghose and Kees Wapenaar, Delft University of Technology*

SUMMARY

Single-well reflection imaging using sonic logging data successfully locates fine-scale structures around a borehole including fractures. In order to achieve accurate and quantitative estimation of fracture properties with high resolution, we propose to couple least-squares migration with linear slip theory. The proposed least-squares migration solves linearized waveform inversion where the wavefield is approximated using a Born operator incorporating a linear slip boundary condition. Representing a fracture as a linear slip interface is advantageous in accurate seismic wave modeling and efficient estimation of fracture properties. We derive conventional elastic least-squares migration for imaging perturbations in elastic constants, and new elastic least-squares migration for imaging fracture compliances. The two formulations are tested using numerical modeling where a dipping fracture is embedded in random background medium. The results show that least-squares migration generally produces higher resolution images for both SH and P-SV wavefields than using adjoint operators. Furthermore, it shows the potential of quantitative estimation of fracture compliances which can be further used in interpreting fracture properties, e.g., fracture infill material and surface condition. The proposed approach, therefore, will be crucial in fracture characterization around a borehole.

INTRODUCTION

Fractures in rocks dominate the hydraulic and mechanical properties in the subsurface. Imaging and characterization of fractures is, therefore, of vital importance in applied geophysics. One of the successful seismic methods for fracture characterization is the detection of seismic anisotropy in combination with the effective medium theory (e.g., Tsvankin et al., 2010), which assumes that the seismic wavelength is much larger than the size and spacing of individual fractures. When those of target fractures are larger or comparable to the seismic wavelength (e.g., high-frequency data or large fractures), alternative methods exist to address physical properties of individual fractures exploiting reflected/scattered waves in surface seismic and borehole seismic configurations (e.g., Beydoun et al., 1985; Willis et al., 2006; Minato et al., 2017, 2018a).

Recently, single-well reflection imaging where sources and receivers are installed in the same borehole receives ample attention. Owing to the developments of directional multipole acoustic tools and sophisticated filtering approaches (e.g., Li and Yue, 2017; Li et al., 2017), single-well imaging enables to locating fine-scale structures around a borehole including fractures up to a few tens of meters away from the borehole (e.g., Tang and Patterson, 2009; Lee et al., 2019). This shows the possibility of high-resolution imaging and quantitative characterization of in-situ individual fractures.

In order to image structures around a borehole, several migration methods have been tested in the context of single-well imaging, e.g., Kirchhoff depth migration, pre-stack f-k migration, beamforming migration, and reverse-time migration (Hornby, 1989; Tang and Patterson, 2009; Li and Yue, 2015; Gong et al., 2018). The fracture imaging was also tested using the reverse time migration in combination with a thin-layer fracture model (e.g., Li et al., 2014; Zhang et al., 2015).

In this study, we propose to couple least-squares migration (e.g., Nemeth et al., 1999) with the linear slip theory (Schoenberg, 1980) for high-resolution quantitative fracture imaging in borehole acoustic settings. Least-squares migration is well established in surface seismic configuration and offers high-resolution images for finite recording aperture, coarse source or receiver sampling and irregular recording gaps (Nemeth et al., 1999). Furthermore, we propose to utilize linear slip theory to accurately represent seismic responses due to fractures and efficiently parameterizing fracture properties in quantitative imaging. A key component in deriving least-squares migration for linear slip interfaces is to obtain the Born or Kirchhoff approximation to the scattered wavefield due to such interfaces. To this end, we use a boundary-integral representation for Green's functions including linear slip interfaces (Wapenaar, 2007). Minato et al. (2018b) have investigated the accuracy of the Born approximation and have shown preliminary Born inversion results considering P-SV waves and a surface seismic configuration. In the following, we first discuss the key concept of using linear slip theory in fracture imaging, and then derive the conventional and new elastic least-squares migrations. Finally we test the two different formulations using numerical modeling.

LINEAR SLIP THEORY IN SEISMIC MODELING AND IMAGING OF FRACTURES

The linear slip theory considers the following boundary condition at a fracture:

$$\Delta\mathbf{u} = \mathbf{Z}\mathbf{t}, \tag{1}$$

where $\Delta\mathbf{u}$ is a seismic-displacement discontinuity across the fracture, $\mathbf{t}$ is a traction vector at the fracture, and $\mathbf{Z}$ is a compliance matrix. In the simplest case of a rotationally invariant fracture (Schoenberg, 1980), $\mathbf{Z}$ is a function of two principal components, i.e., $\mathbf{Z} = diag(\eta_T, \eta_T, \eta_N)$ where η_T is tangential compliance and η_N normal compliance. The unit of the fracture compliance is m/Pa. The fracture compliances can handle structures at a fracture much smaller than the seismic wavelength, e.g., asperities at fracture surfaces and elasticity of fracture infill materials (Worthington and Hudson, 2000). The model also includes a simple thin-layer model, i.e., $\eta_N = h/(\lambda + 2\mu)$ and $\eta_T = h/\mu$ where h is the thickness of a fracture, and λ and μ are Lamé parameters of the thin layer.

A number of laboratory and field experiments suggest that the linear slip model represents well the wave propagation across thin, compliant zones in elastic materials including fractures (e.g., Pyrak-Nolte et al., 1990; Nagy, 1992; Worthington and Hudson, 2000). Furthermore, Nakagawa et al. (2000) show the presence of coupling compliance (off-diagonal components in $\mathbf{Z}$) due to a shear-induced coupling change at the rough surface of a fracture. Such phenomenon is not explained by a simpler fracture model, e.g., the isotropic thin-layer model. Therefore, linear slip model is accurate in modeling seismic wave propagation involving fractures.

The linear slip model has an advantage in quantitatively imaging fractures. The seismic wavelength is often much larger than the thickness of a fracture. When we use a conventional formulation estimating the spatial distribution of elastic constants (e.g., elastic least-squares migration from Beydoun and Mendes, 1989), it would be necessary to represent the imaging volume to be fine enough to capture thickness variation at the fracture. This is prohibited given the current computation capability and is also inefficient considering limited resolution due to available frequency bandwidth. The linear slip theory naturally handles the ambiguity to the seismic wavefield because it is a function of fracture thickness and elasticity of fracture infill material (e.g., $\eta_T = h/\mu$ in the special case of a thin-layer model). Note that the fracture compliances have a clear physical definition and their values are useful for interpretation, e.g., the presence of fluid in fractures (e.g., Lubbe et al., 2008) and slip behaviour at faults (Kame et al., 2014). Therefore, we argue that the use of the linear slip model is accurate, efficient and useful in quantitative fracture imaging.

THEORY

Least-squares migration

Least-squares migration is a linearized waveform inversion (e.g., Nemeth et al., 1999) considering the following relation:

$$\mathbf{d} = \mathbf{L}\mathbf{m}, \tag{2}$$

where $\mathbf{d}$ denotes the seismic data, $\mathbf{L}$ the Born or Kirchhoff operator, and $\mathbf{m}$ the model parameters depending on the linearization. In this study, we consider two different formulations, i.e., a conventional formulation where $\mathbf{m}$ contains the perturbations in elastic constants ($\Delta\lambda$ and $\Delta\mu$), and a new formulation for linear slip interfaces where $\mathbf{m}$ contains the fracture compliances (η_N and η_T). We consider the Born operator for both formulations. The former formulation, i.e., the elastic least-squares migration/inversion using the Born approximation is presented in Beydoun and Mendes (1989). Furthermore, the accuracy of the Born approximation in multipole borehole acoustics is discussed in Geerits et al. (2013). The latter formulation, i.e., a new elastic least-squares migration using linear slip theory requires the Born approximation incorporating linear slip interfaces, which is shown in the next subsection.

Least-squares migration estimates $\mathbf{m}$ by calculating the generalized inverse of the operator $\mathbf{L}$, i.e., $\mathbf{L}^{-g}$. It is often solved using regularization, e.g., conjugate-gradient method with Tikhonov regularization or the model smoothness (e.g., Nemeth et al., 1999; Kühl and Sacchi, 2003). In this study, however, we use an alternative approach to obtain $\mathbf{L}^{-g}$ using the truncated singular-value decomposition (SVD) or natural generalized inverse (Menke, 1989). This enables us to compare imaging results using different formulations (conventional elastic constants or linear slip interfaces) with simple objective criteria without calculating the smoothness in different model parameters. To briefly explain this idea, we consider SVD of $\mathbf{L}$ as $\mathbf{L} = \mathbf{U}\mathbf{S}\mathbf{V}^{\dagger}$, where $\mathbf{U}$ and $\mathbf{V}$ are unitary matrices containing eigenvectors, $\mathbf{S}$ a rectangular diagonal singular-value matrix, and $\dagger$ indicates Hermitian conjugation. The truncated SVD solution of $\mathbf{L}^{-g}$ is $\mathbf{V}_p\mathbf{S}_p^{-1}\mathbf{U}_p^{\dagger}$, where p denotes the rank of $\mathbf{L}$ and the matrices are truncated using the rank p. We select the rank p such that the data residual or the length of null vector in the data space ($S_0(\mathbf{d})$, Menke, 1989) is almost identical in different formulations, assuming that the data contain errors and that a part of the data is not fitted in the inversion. In this way, we present the imaging results from different formulations which almost equally well explain the data.

Born approximation to scattered wavefield due to linear slip interfaces

In this study, we consider wave propagation in a 2D plane which is formed by borehole axis and fracture normal (x-z plane in Figure 1(a)), and we separately consider P-SV and SH wavefields where horizontally oriented sources and receivers are modeled (i.e., dipole sources and receivers). Achieving the coordinate system on the tool requires the knowledge of azimuth angle of target fractures. A recent study shows successful detection of unknown fracture azimuth by rotating the cross-dipole data (Lee et al., 2019). We assume that the P-SV and SH wavefields can be constructed using the approach, or acquisition is designed for specific fracture(s) whose azimuth is known. Extension of our approach to full 3D is also straightforward.

From a convolution-type representation for Green's functions including linear slip interfaces (Wapenaar, 2007), we obtain the following Born approximation to the boundary integral representation in the space-frequency domain:

$$\hat{\mathbf{u}}^{(S)}(\mathbf{x}_r) = -\sum_i \int_{\partial \mathrm{D}_{\mathrm{int}}^{(i)}} \hat{\bar{\mathbf{G}}}(\mathbf{x}_r, \mathbf{x}) \Delta \hat{\mathbf{H}}^{\mathrm{b}}(\mathbf{x}) \hat{\bar{\mathbf{u}}}(\mathbf{x}) d\mathbf{x}, \tag{3}$$

where the boundary $\partial \mathrm{D}_{\mathrm{int}}$ indicates the geometry of the linear slip interface (a fracture), and $\hat{\mathbf{u}}(\mathbf{x}_r)$ is the wave vector at a receiver position $\mathbf{x}_r$ consisting of particle velocities and stress components as $\hat{\mathbf{u}} = (\hat{v}_x\ \hat{v}_z\ -\hat{\tau}_{xx}\ -\hat{\tau}_{zz}\ -\hat{\tau}_{xz})^{\mathsf{T}}$ for the P-SV wavefield, and $\hat{\mathbf{u}} = (\hat{v}_y\ -\hat{\tau}_{xy}\ -\hat{\tau}_{yz})^{\mathsf{T}}$ for the SH wavefield. The superscript S indicates the scattered wavefield, i.e., the difference between the total response and reference response. The bar represents that the quantities are derived from the reference medium. The Green's matrix $\hat{\bar{\mathbf{G}}}(\mathbf{x}_r, \mathbf{x})$ consists of Green's functions at $\mathbf{x}_r$ due to a source at $\mathbf{x}$ (Wapenaar, 2007). The contrast function $\Delta\hat{\mathbf{H}}^{\mathrm{b}}(\mathbf{x})$ contains the fracture compliances (η_T and η_N for the P-SV wavefield, and η_T for the SH wavefield) and dip angle of the fracture. The summation represents the contribution of multiple fractures (see Minato et al., 2018b).

We construct equation 2 from equation 3 such that the data $\mathbf{d}$ contains horizontal particle velocity (v_x for the P-SV wavefield, v_y for the SH wavefield) and the model parameter $\mathbf{m}$ con-

tains the fracture compliances at every grid point. For simplicity, here we ignore the presence of the fluid-filled borehole. The source radiation pattern and receiver reception pattern for the dipole sources and receivers have been investigated (e.g., Tang et al., 2014; Gong et al., 2014), which can be implemented in the proposed approach.

NUMERICAL MODELING EXAMPLES

Model and data

We consider a borehole intersecting a fracture with an angle of 50° (Figure 1(b)) which is embedded in an isotropic elastic background with random heterogeneity. The background heterogeneity is inspired from the work of Tang et al. (2016) where they investigate the effect of scattering in a borehole environment. The random heterogeneity follows von Karman autocorrelation function with Hurst number 1, correlation length 0.1 m, and the amplitude of 10 %. The V_P-V_S ratio is fixed to be 1.74. Scattering due to the random heterogeneity is treated as noise in our numerical tests where Green's functions in least-squares migration are derived from a homogeneous medium.

The fracture is modeled as a linear slip boundary with $\eta_T = 1 \times 10^{-11}$ m/Pa and $\eta_N = 1 \times 10^{-12}$ m/Pa. A fluid-filled fracture with rough surface is assumed, and the normal to tangent compliance ratio is taken from the laboratory experiments (Lubbe et al., 2008). The order of magnitude of fracture compliances is scale dependent (e.g., Hobday and Worthington, 2012); we consider the compliance magnitude assuming the fracture length to be a few tens of meters.

As discussed earlier, we separately model P-SV and SH wavefields. We use the FDTD method incorporating linear slip boundaries (Coates and Schoenberg, 1995). In order to model dipole source measurements, we model horizontal force sources and receivers recording horizontal particle velocities. The source wavelet is a Ricker wavelet with 3 kHz centre frequency. The receiver array consists of 5 receivers with minimum offset of 3 m and receiver spacing of 15 cm. The tool shifts along the borehole axis in steps of 0.5 m. Figure 1(c) shows the first and last source-receiver configurations.

Figures 2(a) and 2(b) show, respectively, the examples of the forward modeled waveform of SH wavefield and P-SV wavefield, for the first receiver with varying source depths (i.e., common receiver gather). Extracting reflection events by filtering direct body and borehole waves is crucial in single-well imaging, which requires careful analyses (e.g., Li and Yue, 2017; Li et al., 2017). For simplicity, in this study, we subtract the response of the reference homogenous medium without the fracture or the random heterogeneity from the total response. The reference homogeneous medium has the average P and S wave velocity of the background medium. The response of the reference medium (Green's functions) is also utilized in least-squares migration.

Figures 2(a) and 2(b) show that the direct waves remain (e.g., at 2 ms in 0 – 6 m in Figure 2(a)) due to insufficient subtraction resulting from the random heterogeneity. The event around 2 ms in 7 – 10 m is the transmitted wave across the fracture.

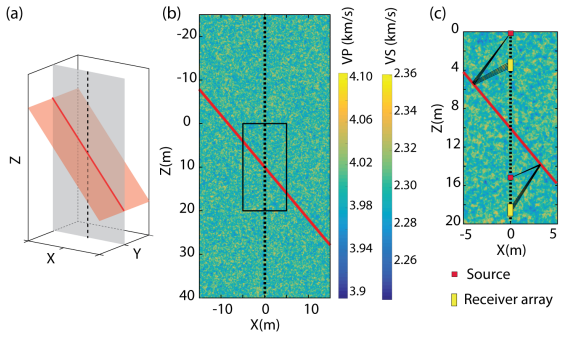

Figure 1: (a) The definition of coordinates and the geometry of borehole (dashed line), fracture surface (red surface), and a 2D x-z plane (gray surface) considered in the numerical modeling. The red line shows the intersection of the fracture surface to the 2D plane. (b) Velocity model in the whole computational volume. A black rectangle shows the imaging area. (c) First and last source-receiver configurations in the imaging area. The ray paths of specular reflections are also shown.

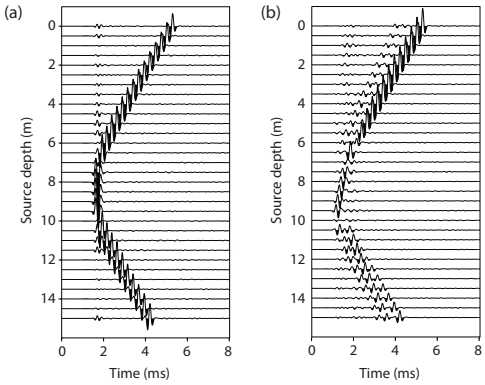

Figure 2: (a) Recorded waveforms for the SH wavefield (horizontal particle velocity) at the first receiver. Scattered waves are shown. (b) Same as (a) but for the P-SV wavefield.

The dipping events in Figure 2 are reflected waves from the fracture. Due to the mode conversion, furthermore, the P-SV wavefield (Figure 2(b)) shows a more complex signature than the SH wavefield (Figure 2(a)).

Inversion results

We apply least-squares migration to the modeled data. Considering the sensitivity of dipole data to shear-wave velocity structures, we image the tangential compliance (η_T) using the proposed formulation (operator $\mathbf{L}_\eta$), or image the shear modulus ($\Delta\mu$) using the conventional formulation (operator $\mathbf{L}_\mu$, e.g., Beydoun and Mendes, 1989). The normal compliance (η_N) is assumed to be zero.

Figure 3 shows the results of the SH wavefield where we image the fracture compliance (Figure 3(a)) and the shear modulus (Figure 3(c)). We also show the imaging results using the Hermitian transpose operator for each formulations ($\mathbf{L}_\eta^\dagger$ and $\mathbf{L}_\mu^\dagger$) in Figure 3(b) and 3(d) so that one can see how least-squares

migration images are improved compared to standard migration images.

The results of the Hermitian transpose operator (Figure 3(b) and 3(d)) show strong artefacts at x = 0 m because of interference of transmitted waves. The least-squares migration (Figure 3(a) and 3(c)) suppresses the artefact and produces higher resolution images. One can see that conventional formulation (Figure 3(c)) shows an X shaped image indicating ambiguity in the fracture location due to the source-receiver configuration. However, such artefacts are not problematic in practical application where upgoing and downgoing waves are separately imaged (e.g., Hornby, 1989). Nevertheless, the new formulation (Figure 3(a)) does not show this ambiguity and images the correct fracture geometry without wavefield separation. We found that this is because the fracture dip angle which we assume to be known (e.g., from borehole acoustic/optical televiewer and conventional migration images) in the migration operator $\mathbf{L}_\eta$ acts as a filter to suppress the artefacts. The results of the P-SV wavefield (Figure 4) are similar to those of the SH wavefield. Contrary to the SH wavefield, the new formulation (Figure 4(a)) shows an X shaped image. This is mainly because the filtering effect in the operator $\mathbf{L}_\eta$ is not same as in the SH wavefield due to the complex radiation patterns in Green's functions and the additional stress rotation required to handle both η_T and η_N.

Least-squares migration using both formulations successfully estimates the physical parameters at the fracture with high resolution. The imaged values of η_T are underestimated because the Born approximation overpredicts amplitudes (Minato et al., 2018b). The phase of the imaged fracture is opposite in η_T and $\Delta\mu$ because a compliant fracture ($\eta_T > 0$) effectively reduces the shear modulus ($\Delta\mu < 0$). As discussed earlier, those results give almost identical data residuals. However, the effective medium theory (Coates and Schoenberg, 1995) predicts that the inclusion of a dipping linear slip interface in a small volume (much smaller than the seismic wavelength) results in transverse isotropy, which implies the conventional formulation ($\Delta\lambda$ and $\Delta\mu$) produces additional artefacts.

CONCLUSION

We formulate least-squares migration in the context of single-well reflection imaging for dipole measurements. For brevity, we separately consider P-SV and SH wavefields, and we ignore the presence of the borehole. We formulate the conventional elastic least-squares migration for imaging the perturbations of elastic constants, and the new elastic least-squares migration for imaging fracture compliances incorporating linear slip theory. We numerically test the two formulations in imaging a fracture embedded in a random background medium. The results show that the least-squares migration generally produces higher-resolution quantitative images than using the adjoint operator. Because the linear slip theory accurately models the seismic wavefield due to fractures, and parameterizing a fracture using fracture compliances naturally handles ambiguity in fracture thickness and elasticity of the infill materials, the new formulation will be crucial in quantitatively imaging fracture properties.

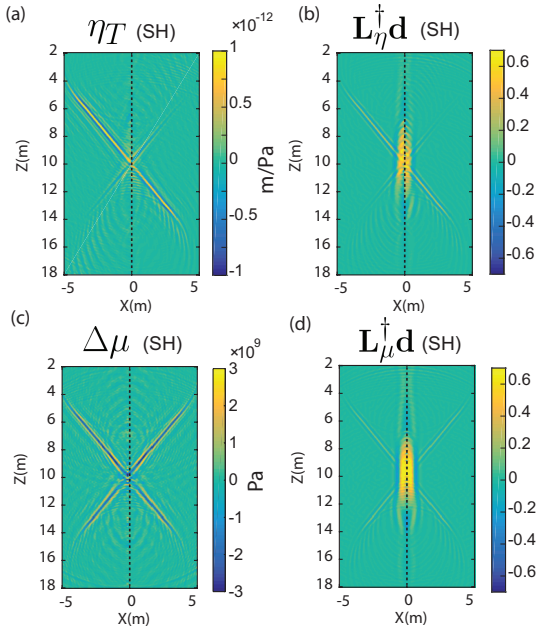

Figure 3: (a) Imaging result of least-squares migration for linear slip interface (η_T) using a SH wavefield. (b) Imaging result of Hermitian conjugate operator of least-squares migration for linear slip interface ($\mathbf{L}_\eta$). (c) Same as (a) but using conventional elastic least-squares migration ($\Delta\mu$). (d) Same as (b) but using the operator from the conventional formulation ($\mathbf{L}_\mu$).

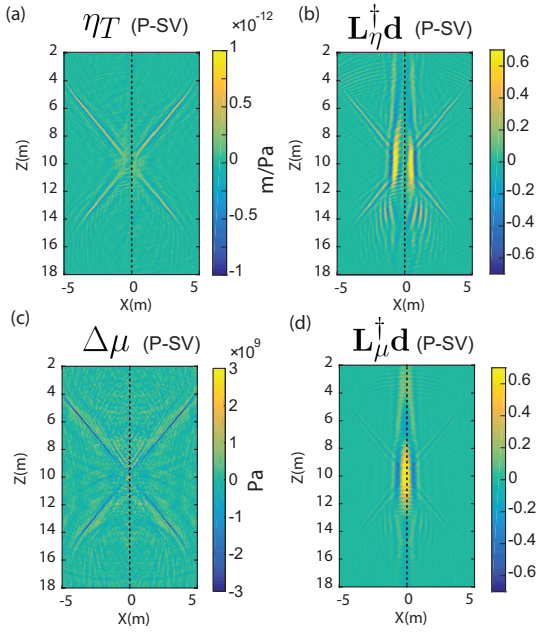

Figure 4: Same as Figure 3 but using a P-SV wavefield. See the caption of Figure 3.

REFERENCES

Beydoun, W., C. Cheng, and M. Toksöz, 1985, Detection of open fractures with vertical seismic profiling: Journal of Geophysical Research: Solid Earth, **90**, 4557–4566.

Beydoun, W. B., and M. Mendes, 1989, Elastic ray-born l2-migration/inversion: Geophysical Journal International, **97**, 151–160.

Coates, R., and M. Schoenberg, 1995, Finite difference modeling of faults and fractures: Geophysics, **60**, 1514–1526.

Geerits, T. W., I. Veile, and O. Hellwig, 2013, Far field elastodynamic Born scattering revisited: Journal of Applied Geophysics, **89**, 141–163.

Gong, H., H. Chen, X. He, C. Su, X. M. Wang, B. C. Wang, and X. H. Yan, 2018, Modeling and inversions of acoustic reflection logging imaging using the combined monopole–dipole measurement mode: Applied Geophysics, **15**, 393–400.

Gong, H., H. Chen, X. He, and X. Wang, 2014, Eliminating the azimuth ambiguity in single-well imaging using 3C sonic data: Geophysics, **80**, A13–A17.

Hobday, C., and M. Worthington, 2012, Field measurements of normal and shear fracture compliance: Geophysical Prospecting, **60**, 488–499.

Hornby, B. E., 1989, Imaging of near-borehole structure using full-waveform sonic data: Geophysics, **54**, 747–757.

Kame, N., K. Nagata, M. Nakatani, and T. Kusakabe, 2014, Feasibility of acoustic monitoring of strength drop precursory to earthquake occurrence: Earth, Planets and Space, **66**, 1–12.

Kühl, H., and M. D. Sacchi, 2003, Least-squares wave-equation migration for AVP/AVA inversion: Geophysics, **68**, 262–273.

Lee, S.-Q., X.-M. Tang, and Y.-d. Su, 2019, Shear wave imaging to determine near-borehole faults for ocean drilling exploration: Geophysical Journal International, **217**, 288–293.

Li, C., and W. Yue, 2015, High-resolution adaptive beamforming for borehole acoustic reflection imaging: Geophysics, **80**, D565–D574.

———, 2017, High-resolution radon transforms for improved dipole acoustic imaging: Geophysical Prospecting, **65**, 467–484.

Li, J., K. A. Innanen, and G. Tao, 2017, Extraction of reflected events from sonic-log waveforms using the Karhunen-Loève transform: Geophysics, **82**, D265–D277.

Li, J., G. Tao, K. Zhang, B. Wang, and H. Wang, 2014, An effective data processing flow for the acoustic reflection image logging: Geophysical Prospecting, **62**, 530–539.

Lubbe, R., J. Sothcott, M. Worthington, and C. McCann, 2008, Laboratory estimates of normal and shear fracture compliance: Geophysical Prospecting, **56**, 239–247.

Menke, W., 1989, Geophysical data analysis: discrete inverse theory: Academic Press.

Minato, S., R. Ghose, and G. Osukuku, 2018a, Experimental verification of spatially varying fracture-compliance estimates obtained from amplitude variation with offset inversion coupled with linear slip theory: Geophysics, **83**, WA1–WA8.

Minato, S., R. Ghose, T. Tsuji, M. Ikeda, and K. Onishi, 2017, Hydraulic properties of closely spaced dipping open fractures intersecting a fluid-filled borehole derived from tube wave generation and scattering: Journal of Geophysical Research: Solid Earth, **122**, 8003–8020.

Minato, S., R. Ghose, and K. Wapenaar, 2018b, Seismic modelling and inversion of nonwelded interfaces using the boundary integral equation: Proceedings of the 13th SEGJ International Symposium.

Nagy, P., 1992, Ultrasonic classification of imperfect interfaces: Journal of Nondestructive Evaluation, **11**, 127–139.

Nakagawa, S., K. Nihei, and L. Myer, 2000, Shear-induced conversion of seismic waves across single fractures: International Journal of Rock Mechanics and Mining Sciences, **37**, 203 – 218.

Nemeth, T., C. Wu, and G. T. Schuster, 1999, Least-squares migration of incomplete reflection data: Geophysics, **64**, 208–221.

Pyrak-Nolte, L., L. Myer, and N. Cook, 1990, Transmission of seismic waves across single natural fractures: Journal of Geophysical Research, **95**, 8617–8638.

Schoenberg, M., 1980, Elastic wave behavior across linear slip interfaces: The Journal of the Acoustical Society of America, **68**, 1516–1521.

Tang, X. M., J. Cao, and Z. Wei, 2014, Shear-wave radiation, reception, and reciprocity of a borehole dipole source: With application to modeling of shear-wave reflection survey: Geophysics, **79**, T43–T50.

Tang, X. M., Z. Li, C. Hei, and Y. D. Su, 2016, Elastic wave scattering to characterize heterogeneities in the borehole environment: Geophysical Journal International, **205**, 594–603.

Tang, X. M., and D. J. Patterson, 2009, Single-well S-wave imaging using multicomponent dipole acoustic-log data: Geophysics, **74**, WCA211–WCA223.

Tsvankin, I., J. Gaiser, V. Grechka, M. van der Baan, and L. Thomsen, 2010, Seismic anisotropy in exploration and reservoir characterization: An overview: Geophysics, **75**, 75A15–75A29.

Wapenaar, K., 2007, General representations for wavefield modeling and inversion in geophysics: Geophysics, **72**, SM5–SM17.

Willis, M., D. Burns, R. Rao, B. Minsley, M. Toksoz, and L. Vetri, 2006, Spatial orientation and distribution of reservoir fractures from scattered seismic energy: Geophysics, **71**, O43–O51.

Worthington, M. H., and J. A. Hudson, 2000, Fault properties from seismic Q: Geophysical Journal International, **143**, 937–944.

Zhang, G., N. Li, H. W. Guo, H. L. Wu, and C. Luo, 2015, Fracture identification based on remote detection acoustic reflection logging: Applied Geophysics, **12**, 473–481.